Comparative study of cluster $Ag_{17}Cu_2$ by instantaneous normal mode analysis and by isothermal Brownian-type molecular dynamics simulation

Ping-Han Tang,[1] Ten-Ming Wu,[1,a)] Tsung-Wen Yen,[2] S. K. Lai,[2,3,b)] and P. J. Hsu[2,3]
[1]*Institute of Physics, National Chiao-Tung University, Hsin Chu, Taiwan*
[2]*Complex Liquids Laboratory, Department of Physics, National Central University, Chungli 320, Taiwan*
[3]*Molecular Science and Technology Program, Taiwan International Graduate Program, Academia Sinica, Taipei 115, Taiwan*

(Received 17 March 2011; accepted 5 August 2011; published online 1 September 2011)

We perform isothermal Brownian-type molecular dynamics simulations to obtain the velocity autocorrelation function and its time Fourier-transformed power spectral density for the metallic cluster $Ag_{17}Cu_2$. The temperature dependences of these dynamical quantities from $T = 0$ to 1500 K were examined and across this temperature range the cluster melting temperature T_m, which we define to be the principal maximum position of the specific heat is determined. The instantaneous normal mode analysis is then used to dissect the cluster dynamics by calculating the vibrational instantaneous normal mode density of states and hence its frequency integrated value I_j which is an ensemble average of all vibrational projection operators for the jth atom in the cluster. In addition to comparing the results with simulation data, we look more closely at the entities I_j of all atoms using the point group symmetry and diagnose their temperature variations. We find that I_j exhibit features that may be used to deduce T_m, which turns out to agree very well with those inferred from the power spectral density and specific heat. © *2011 American Institute of Physics*. [doi:10.1063/1.3628669]

I. INTRODUCTION

Given an n-body empirical potential, one can show[1] that a 13-atom silver cluster has an icosahedral geometry in its lowest energy state. This icosahedral structure is unaffected even if we replace one Ag atom by a Cu atom. The cluster's lowest energy structure remains an icosahedron but in this case the Cu atom occupies the central position of the icosahedron. If one considers a seven-atom cluster comprising six Ag atoms and one Cu atom, its lowest energy structure is a pentagonal bipyramid with the Cu atom residing at one of the apex positions. Interestingly, a 19-atom cluster consisting of 2 Cu atoms and 17 Ag atoms takes on its ground state geometry by simply joining the 7- and 13-atom clusters in which the Cu atom in the 7-atom cluster substitutes one of the apex atoms in the 13-atom cluster thus forming a double icosahedron. The 19-atom bimetallic cluster (BC), $Ag_{17}Cu_2$, is therefore characterized by two "center" atoms Cu locating inside 17 "surface" atoms Ag and the atoms assume a geometry of a double icosahedron. This lowest energy structure is consistent with our understanding of a BC that an atom of smaller size (ionic radii of Cu and Ag are 0.96 Å and 1.26 Å, respectively) prefers to be surrounded by atoms of larger size. This mixing tendency arises from the size-mismatched disparity and has previously been noted in the literature for the noble-metal-based BCs.[1–3]

This paper is concerned with a study of the cluster dynamics of this 19-atom double icosahedron. Our motivation comes from a recent work of Yen *et al.*[4] who reported simulation results on 14-atom Ag-based BCs. In their work, they applied the isothermal Brownian-type molecular dynamic (MD) simulations to the latter class of BCs and calculated the velocity autocorrelation function (VAF) and its Fourier-transformed power spectral density $\Omega^{(i)}(\omega)$, the superscript i being the ith atom in the cluster. Starting from the lowest energy state, which consists of an adatom Ag sitting outside an icosahedron in which is embbedded at its center of an "impurity" atom Cu, for $Ag_{13}Cu_1$ or Au for $Ag_{13}Au_1$, the BC is heated up to high temperatures. Two specific features in the $\Omega^{(i)}(\omega)$ of these BCs were observed. First, the impurity atom Cu or Au has two distinct frequency modes: a lower frequency mode with a value slightly higher than the frequency modes of Ag atoms (which all share an average same frequency (see Figs. (8)–(13) in Ref. 4) and a well-separated higher frequency mode which occurs solely for the Cu or Au atom. Second, the magnitude of $\Omega^{(i)}(\omega)$ at the higher frequency mode of the Au atom is relatively lower and does not change much ($\Omega^{(i)}(\omega) \approx 1.25$ Å^2/ps) with increasing temperature and this thermal variation is in marked contrast to that of Cu atom showing a distinctly high peak with increasing temperature. This latter feature is interesting if we compare these thermal characteristics with the 14-atom pure Ag cluster whose magnitude of the $\Omega^{(i)}(\omega)$ at the higher frequency mode declines gradually as the temperature rises and disappears identically at a certain high temperature. While these two notable features may be taken as emphatic criteria to estimate the melting temperatures T_m for Ag_{14}, $Ag_{13}Au_1$, and $Ag_{13}Cu_1$ and the inferred T_m are generally satisfactory in comparison to those deduced from their corresponding specific heat C_V data, these authors did not

a)Electronic mail: tmw@faculty.nctu.edu.tw.
b)Electronic mail: sklai@coll.phy.ncu.edu.tw.

offer a corroborative interpretation of the complex frequency modes which clearly show up at different ranges of temperature. The thermal effect that gives rise to the microscopic cluster dynamics thus remains an issue worthwhile further investigation.

In this work, in addition to applying the same MD technique to $Ag_{17}Cu_2$ to obtain VAF and $\Omega^{(i)}(\omega)$, we analyze the simulation data in the context of instantaneous normal mode (*INM*) concept which is an approach originally motivated for understanding the short-time dynamics of liquids from the point of view of the potential energy landscape.[5,6] Considerable efforts have been devoted in recent years to transpose the INM theory into an analytic tool and in this context fruitful dynamic properties of bulk systems have in fact been reported for simple liquids,[7,8] amorphous materials,[9] biological systems,[10] etc. On the other hand, the analyses for cluster dynamics and thermodynamics from the viewpoint of potential energy landscape have been developed independently.[11,12] In a series of papers in 1990, Stratt and Adams[13–15] have advanced using the strategy of INM for clusters. These series of works have been inspired conceptually by the so-called inherent structures in a liquid[16,17] and by early theoretical attempts of Berry *et al.*,[18–28] who developed statistical mechanical models for clusters, studied the various cluster dynamical properties and the finite-sized effect on cluster melting, and corroborated their findings by comparing them with the simulation data of argon clusters. Despite the insight provided by the theory of INM, the tactics to exploit the cluster dynamics with the INM analysis remains an endeavor to be further explored. The major impediment lies in the particle number. Whereas in the bulk system the particle number is infinite in the thermodynamic limit, the particle number in the cluster is, however, finite. Even with a cluster that contains less than a hundred number of particles, its energy landscape has a complex multi-dimensional space. One fundamental and unique feature for a cluster is that it has rotational motions about three principal axes. This unique trait for clusters causes the INM in some aspects different from the bulk systems. Below we shall first give a general review of the INM and indicate the particular aspects that are specific to clusters.

This paper is organized as follows. In Sec. II, we summarize the technical details of the isothermal Brownian-type MD simulation and give the empirical n-body potential that we employ to calculate the thermal and dynamical properties. In the same section, the formulas of C_V, VAF, and its Fourier-transformed power spectral density will be given as well. The INM for clusters will also be described in a subsection here, too. Section III presents our results of calculations for $Ag_{17}Cu_2$ and for comparison includes also $Ag_{12}Cu_1$. We deduce in particular the melting temperature T_m from C_V and compare the estimated value with the one inferred from the power spectral density. We analyze the dynamics of $Ag_{17}Cu_2$ at different temperatures by means of INM and compare the frequencies obtained from the latter with those appearing in $\Omega^{(i)}(\omega)$. With the INM, we propose a new order parameter for describing the melting behavior of $Ag_{17}Cu_2$. A conclusion of our work is given in Sec. IV.

II. THEORY

A. Simulation algorithm

1. Isothermal Brownian-type molecular dynamics

In this section, we give a brief description of the isothermal Brownian-type MD simulation since considerable technical details have been given in Refs. 29–31. As in our previous works, we employ the modified cubic coupling scheme which was originally developed for studying the thermal properties of pure metallic clusters[29] and subsequently generalized to alloy clusters.[30,31] Let us consider a bimetallic cluster $A_{n_a}B_{n_b}$, where n_a (n_b) is the number of atoms of a-type (b-type). The equations of motion, which describe its x-component at a temperature T, can be written as

$$\dot{x}_{i_a} = \frac{p_{i_a,x}}{m_a}, \tag{1}$$

$$\dot{p}_{i_a,x} = -\frac{\partial E_n}{\partial x_{i_a}} - \frac{\alpha_a e_{0,a}}{nL_0}\mu_{a,x}^3 \frac{p_{i_a,x}}{\tilde{p}_{0,a}} - \frac{\beta_a e_{0,a}}{nL_0}\nu_{a,x}\left(\frac{p_{i_a,x}^2}{\tilde{p}_{0,a}^2} - d_0\right) - \frac{\vartheta_a e_{0,a}}{nL_0}\eta_{a,x}\frac{p_{i_a,x}^3}{\tilde{p}_{0,a}^3}, \tag{2}$$

in which x_{i_a} and $p_{i_a,x}$ are the x-component position coordinate and momentum, respectively, and the subscript i_a refers to the ith atom of type a. The variables $\mu_{a,x}$, $\nu_{a,x}$, and $\eta_{a,x}$ are the x-component pseudo-friction coefficients of a-type atom and they are introduced to simulate the heat bath degrees of freedom. The entities L_0 and $e_{0,a}$ are constant parameters and α_a, β_a, ϑ_a, and $\tilde{p}_{0,a}$ are all functions of T. For b-type atoms, we simply replace the subscript a by b in Eqs. (1) and (2). The same set of equations hold for the y and z components. The explicit expressions of all of these quantities and the detailed numerical procedure to be effected are well described in Refs. 29–31 to which the interested readers are referred.

2. Empirical n-body Gupta potential

Intrinsically, the interactions between atoms in a cluster are many-body in nature. The inextricable complexity of Coulomb interactions between valence electrons and ions renders a first-principles derivation of a many-particle potential energy function a formidable task. Here, we employ the n-body Gupta potential[32] function, which is widely accepted in the literature as a substitution. This empirical potential can be written as

$$E_n = \sum_{i=1}^{n}\left\{\sum_{j=1(j\neq i)}^{n} A_{ij}\exp\left[-p_{ij}\left(\frac{r_{ij}}{r_{ij}^{(0)}}-1\right)\right] - \left[\sum_{j=1(j\neq i)}^{n}\xi_{ij}^2\exp\left(-2q_{ij}\left(\frac{r_{ij}}{r_{ij}^{(0)}}-1\right)\right)\right]^{1/2}\right\}. \tag{3}$$

The parameters A_{ij}, p_{ij}, q_{ij}, ξ_{ij}, and $r_{ij}^{(0)}$ for the Ag–Cu are obtained from the work of Mottet *et al.*[33] and are given in Table I.

TABLE I. Gupta-type potential parameters for the bimetallic clusters Ag–Cu taken from Mottet *et al.* (Ref. 33). The $r_{ij}^{(0)}$ for Ag–Cu is calculated by averaging the $r_{ij}^{(0)}$ of Ag–Ag and Cu–Cu.

ij	A_{ij}				$r_{ij}^{(0)}$
ij	(eV)	ξ_{ij}	p_{ij}	q_{ij}	(Å)
Cu–Cu	0.0894	1.2799	10.55	2.43	2.56
Ag–Cu	0.0977	1.2275	10.7	2.805	2.725
Ag–Ag	0.1031	1.1895	10.85	3.180	2.89

B. Thermal property: Specific heat

For the thermal property, we calculate the specific heat C_V. The computation of this quantity is straightforward since the configuration energies were readily recorded by the above equations. Following our previous works,[29,30] we compute

$$C_V = \frac{\langle E_{total}^2 \rangle_t - \langle E_{total} \rangle_t^2}{k_B T^2}, \tag{4}$$

where $E_{total} = (\sum_{i_a=1}^{n_a} p_{i_a}^2 / 2m_a + \sum_{i_b=1}^{n_b} p_{i_b}^2 / 2m_b) + E_n$ in which E_n is given by Eq. (3) by taking the time average (see Eq. (10) in Ref. 29). To determine the melting temperature of a cluster, we begin at $T = 0$ K and heat it up to high temperatures. The temporal variations of the position coordinates of all atoms in the BC at different T are then recorded. Rather long elapsed times in the range of $(1-3) \times 10^{-7}$s were performed so that the calculated C_V vs. T curve develops as smooth as possible. Any larger fluctuation that still remains would indicate the necessity to improve the modified cubic coupling scheme.

C. Dynamical property: Velocity autocorrelation function and power spectrum

The displacement of atoms in a cluster has to be bounded (which implies a zero diffusion constant) and cannot, therefore, continue to increase with time[13] as in the bulk liquids whose diffusion shows the asymptotic behavior of growing linearly with time. As a result, there remains an ambiguity in the study of the dynamical properties of a cluster that resorts to the mean-square displacement of atoms. A more useful dynamical quantity to examine is perhaps the VAF, which is defined by

$$C(t) = \frac{\sum_{i=1}^{n} \sum_{j=1}^{M} \vec{\mathbf{v}}_i(t_{0j}) \cdot \vec{\mathbf{v}}_i(t_{0j}+t)}{\sum_{i=1}^{n} \sum_{j=1}^{M} \vec{\mathbf{v}}_i(t_{0j}) \cdot \vec{\mathbf{v}}_i(t_{0j})}, \tag{5}$$

where $n = n_a + n_b$ is the total number of atoms in a BC containing n_a (n_b) atoms of type a (b) and M is the number of time origins t_{0j} taken along an ergodic trajectory. Keeping track on $C(t)$ as a function of temperature, one would be able to see it changing generally from a solidlike vibrational behavior at low temperatures, where $C(t)$ exhibits robust oscillation to a structural profile at high enough temperatures by one conspicuous minimum followed by a decaying tail. The former structure of $C(t)$ is due to atoms executing incessant vibrations about latticelike locations in the cluster which result in the $\vec{\mathbf{v}}(t_{0j}+t)$ changing in magnitude and direction, whereas the latter structure of $C(t)$ comes from additional diffusive movements since atoms in the liquidlike phase are not fixed in positions. There is another complication for a cluster. At low temperatures before melting, there might already occur different kinds of atomic activities. Consider, for instance, a 14-atom cluster. It comprises an icosahedron and a "floating" atom residing outside. Due to its location outside the icosahedron, the floating atom interacts weakly with its neighboring atoms and is thus relatively free to wander about experiencing, for example, a kind of migrational relocation from one (symmetrical) site to another. Since the amount of energy required for such a relocation is generally small, the adatom may just effect the migrational relocation at a lower temperature. Depending on the kind of cluster under studied, we observe (via video) different dynamic motions for the adatom for different clusters. For example, at low temperatures in cluster Ag_{14}, its adatom *moves toward* the icosahedron enhancing its interactions with the surface atoms, whereas for $Ag_{13}Cu_1$ at the same temperatures its adatom *wheels circumferentially* threading along the nearby atoms facing it. As a result of these general behaviors, the Ag_{14} cluster undergoes exchange of sites between the adatom and surface atoms at a temperature relatively lower ($T \approx 130$ K) than the $Ag_{13}Cu_1$ ($T \approx 170$ K). This difference in migrational relocation motion reduces, however, at much higher temperatures. Thus, a quantitative and deeper insight into the microscopic dynamics is not to dissect the temperature dependences of the characteristic of the whole cluster $C(t)$ but to trail instead the individual atoms since atoms in a cluster are distributed with varying neighbors. Accordingly, we consider

$$C^{(i)}(t) = \frac{\sum_{j=1}^{M} \vec{\mathbf{v}}_i(t_{0j}) \cdot \vec{\mathbf{v}}_i(t_{0j}+t)}{\sum_{j=1}^{M} \vec{\mathbf{v}}_i(t_{0j}) \cdot \vec{\mathbf{v}}_i(t_{0j})}, \tag{6}$$

which is the normalized VAF for the ith atom in a BC. That $C^{(i)}(t)$ is preferred to $C(t)$ is based on the recognition that in studies of bulk systems the average over atoms in $C(t)$ is carried out to improve the statistical accuracy since the dynamical motion for each of all atoms is assumed the same in bulk systems. We note further two points. First, we have defined a normalized $C^{(i)}(t)$ in Eq. (6) for the reason that the small-time limit of VAF is inversely proportional to the mass of the atom.[34] Second, we have corrected the velocities of atoms for the translational as well as the rotational motion of the whole cluster. Failing to make these corrections will result in a non-zero value of the long-time limit of $C^{(i)}(t)$. Having introduced $C^{(i)}(t)$, another useful function is the power spectrum,

$$\Omega^{(i)}(\omega) = 2 \int_0^\infty C^{(i)}(t) \cos(\omega t) dt. \tag{7}$$

This function reveals the vibrational behavior of atoms, which may be used to project out the underlying frequencies of the individual atomic processes. When $\Omega^{(i)}(\omega)$ of all atoms share a same frequency, say ω_L, the ω_L is reminiscent of the infrared molecular vibration. On the other hand, we know in bulk materials the low frequency limit of $\Omega^{(i)}(\omega)$ pertains to the diffusion coefficient, which is non-zero for atoms in a liquid phase. This latter trait is yet to be clarified[13,31] for a

finite-sized system. Nevertheless the simulated power spectra for the BCs considered here appear to preserve this feature as we will see shortly in the following calculated results. The characteristic changes of $C^{(i)}(t)$ and $\Omega^{(i)}(\omega)$ with temperature will be illustrated below for $Ag_{17}Cu_2$.

We remark furthermore at this point that in actual simulation runs the C_V at each T (at interval ΔT =5–10 K) was calculated for a total elapsed time $t_{tot} \geq 0.2 \times 10^{-7}$s, whereas for VAF the simulation run was effected at ΔT =100 K for $t_{tot} \geq 1 \times 10^{-9}$s with at least $M = 99 \times 10^4$ time origins (see Eqs. (5) and (6)).

D. Dynamical property: Instantaneous normal modes analysis

This subsection is devoted to describing the method of INM and using it to study the dynamics of metallic clusters. Consider a cluster of n metallic atoms with mass m_j ($j = 1, \ldots, n$ which may be of different species). These atoms occupy position vectors $\boldsymbol{R} \equiv (\boldsymbol{r}_1, \ldots, \boldsymbol{r}_n) = (r_{1x}, r_{1y}, r_{1z}, \ldots, r_{nx}, r_{ny}, r_{nz})$. If the interactions among atoms are described by the many-body empirical Gupta potential,[32] the potential energy $V(\boldsymbol{R})$ of the cluster evaluated at $\boldsymbol{R}$ is a function in $3n$-dimensional space. For given configuration $\boldsymbol{R}$, one may construct a $3n \times 3n$ Hessian matrix $\boldsymbol{K}(\boldsymbol{R})$ by the formula,[35]

$$K_{i\mu,j\nu}(\boldsymbol{R}) = \frac{1}{\sqrt{m_i m_j}} \left(\frac{\partial^2 V(\boldsymbol{R})}{\partial r_{i\mu} \partial r_{j\nu}} \right)_{\boldsymbol{R}}, \tag{8}$$

where $i\mu$ ($j\nu$) refers to the atom i (j) that in Cartesian coordinates takes on $\mu = x, y, z$ ($\nu = x, y, z$). In Eq. (8), we have defined $\boldsymbol{K}(\boldsymbol{R})$ in mass-weighted Cartesian coordinates in a form that allows the description of atoms of different species. With reference to the specific configuration $\boldsymbol{R}$, the eigenmodes of $\boldsymbol{K}(\boldsymbol{R})$, $\alpha = 1, \ldots, 3n$, are referred to as the INM of the n atoms. The eigenvalues of the Hessian matrix $\boldsymbol{K}(\boldsymbol{R})$ are the frequencies ω_α^2 of the INMs, which, of course, depend on $\boldsymbol{R}$. The normalized eigenvectors of the $3n$ eigenmodes are denoted by $\vec{e}_j^{\,\alpha}$, being the three-dimensional displacement vector of the jth atom in the α mode of INMs. Since the configurations at which the Hessian matrices are evaluated may not correspond in general to the local minima of $V(\boldsymbol{R})$, the eigenvalues are not guaranteed positive definite and the normal mode frequencies ω_α may thus be either real or imaginary.

Among the INM, there are three zeros which correspond to the three-dimensional translational motion of the center-of-mass of the atoms. For the bulk system, such as a liquid or glass, the remaining INMs describe the vibrational motions of the atoms, whereas for the finite-sized system such as a cluster which composes of given number of atoms, the remaining INMs include contributions from the three rotational degrees of freedom of the whole cluster in addition to vibrations and hence $3n - 6$ vibrational degrees of freedom. This unique feature of the rotational contribution to the remaining INMs can be separated out generally by two methods. In one method, referred as *method I* in this paper, the clusters are assumed to have an extremely weak rotation-vibration coupling and the procedure is to use the standard projection technique[15,36] in which a $3n \times 3n$ projection matrix $\boldsymbol{Q}(\boldsymbol{R})$ is constructed from three purely rotational eigenvectors $\vec{e}_j^{\,\alpha}$ (see Appendix A) defined by

$$Q_{i\mu,j\nu}(\boldsymbol{R}) = \sum_{\alpha = R'_x, R'_y, R'_z} e_{i\mu}^{\alpha} \cdot e_{j\nu}^{\alpha},$$

where $e_{j\nu}^{\alpha}$ is the Cartesian component of the eigenvector $\vec{e}_j^{\,\alpha}$ with $\nu = x, y, z$. To project out the rotational degrees of freedom, one defines a projected Hessian matrix as

$$\boldsymbol{K}^{(p)}(\boldsymbol{R}) = [\boldsymbol{I}_{3n} - \boldsymbol{Q}(\boldsymbol{R})] \cdot \boldsymbol{K}(\boldsymbol{R}) \cdot [\boldsymbol{I}_{3n} - \boldsymbol{Q}(\boldsymbol{R})],$$

where $\boldsymbol{I_{3n}}$ is the $3n \times 3n$ unit matrix. The diagonalization of $\boldsymbol{K^{(p)}}(\boldsymbol{R})$ then yields purely vibrational eigenvectors with nonzero eigenvalues. Implicit in this procedure is that the clusters under consideration are close to rigid and their rotational and vibrational degrees of freedom are supposedly decoupled. This method works generally, however, for those clusters in which the rotation-vibration couplings are extremely weak. However, under the INM approximation, the instantaneous rotation of a cluster is considered as a rigid body with the cluster structure at the instant and its total angular momentum is regarded as a constant so that one may simply apply this method for the cluster configurations at every instant.

In another method, referred as *method II*, it was pointed out by Adams and Stratt[15] that the three rotational INMs in the cluster are coupled with the vibrational degrees of freedom resulting in the mixing modes of the former and the extent of mixing increases with cluster temperature. The authors then proposed another projection scheme to separate out the rotational contributions. Technically, one appeals to the three rotational eigenmodes in the Hessian matrix $\boldsymbol{K}(\boldsymbol{R})$ that possess the largest angular momentum values and recognizes that each α mode of $\vec{\boldsymbol{e}}_j^{\,\alpha}$ is proportional to the velocity whose vector property describes the instantaneous directions of the atomic motions in the center-of-mass coordinate system of the cluster. Accordingly, the magnitude of the rotational angular momentum in eigenmode α can be approximated as

$$L_\alpha = c \left| \sum_{j=1}^{n} \sqrt{m_j} (\vec{r}_j \times \vec{\boldsymbol{e}}_j^{\,\alpha}) \right|, \tag{9}$$

where $\vec{r}_j$ is the position vector of the jth atom with mass m_j and c is a proportionality constant between the instantaneous velocities of particles and the normalized INM eigenvector. In this scheme, the rotational INMs, denoted as (R_x, R_y, R_z), are thus recognized as three with the largest L_α values. Here, two remarks are in order. First, with the eigenvectors $\vec{\boldsymbol{e}}_j^{\,\alpha}$ defined above in the mass-weighted form, c is different from the one given in Ref. 15 for atoms with equal mass. Second, the instantaneous cluster motions in the three rotational INMs generally behave as rotations of the whole cluster, although mixing with vibrations is to some extent seen among atoms.

By excluding the three-translational and three-rotational INMs, the normalized vibrational INM density of states (DOS) of a cluster is then written as

$$D_{Vib}(\omega) = \left\langle \frac{1}{3n-6} \sum_{\alpha=1}^{3n-6} \delta(\omega - \omega_\alpha) \right\rangle, \tag{10}$$

where the brackets mean an ensemble average over cluster configurations. Generally, D_{Vib} is divided into two lobes, $D_{Vib}^{(s)}(\omega)$, and $D_{Vib}^{(u)}(\lambda)$, which are the DOS of the vibrational stable-INM (denoted by the superscript s) with real frequencies ω and the vibrational unstable-INM (denoted by the superscript u) with imaginary frequencies $\omega_\alpha = i\lambda_\alpha$, respectively. The normalization of $D_{Vib}(\omega)$ yields a unit area under the curves of $D_{Vib}^{(s)}(\omega)$ and $D_{Vib}^{(u)}(\lambda)$, which are usually plotted in the positive and negative axes of ω, respectively.[6,7]

If the number of time origin in Eq. (5) for $C(t)$ is large enough, the time average in Eq. (5) can reasonably be replaced by an ensemble average over the cluster configurations. This would imply that the $C(t)$ may be connected to the vibrational motions of atoms in the cluster in the context of INM,[37] and we arrive at

$$C(t) \approx \int D_{Vib}(\omega)\cos(\omega t)d\omega = \int_0^\infty D_{Vib}^{(s)}(\omega)\cos(\omega t)d\omega + \int_0^\infty D_{Vib}^{(u)}(\lambda)\cosh(\lambda t)d\lambda. \tag{11}$$

We should point out that the calculation within INM accurately predicts $C(t)$ in the short-time regime; $C(t)$, however, diverges badly in the long-time limit due to the imaginary-frequency term in Eq. (11). In the stable-INM approximation[37,38] in which the contribution due to the imaginary-frequency INM is neglected, the $C(t) \to C_{\mathrm{INM}}^{(s)}$ is further simplified to

$$C_{\mathrm{INM}}^{(s)}(t) = \frac{\int_0^\infty D_{Vib}^{(s)}(\omega)\cos(\omega t)d\omega}{\int_0^\infty D_{Vib}^{(s)}(\omega)d\omega}, \tag{12}$$

where the denominator is a renormalized factor.

To make further progress, we introduce the projection operator P_j^α, which sorts out the INM of the atom j in a cluster with the eigenmode α. In Cartesian coordinates x, y, and z, it reads[35,38]

$$P_j^\alpha = \left|\vec{e}_j^{\,\alpha}\right|^2 = \sum_{\mu=x,y,z} e_{j\mu}^\alpha \cdot e_{j\mu}^\alpha \tag{13}$$

and, due to the normalization of an INM eigenvector, P_j^α obeys the following two sum rules:

$$\sum_{j=1}^{n} P_j^\alpha = 1 \tag{14}$$

and

$$\sum_{\alpha=1}^{3n} P_j^\alpha = 3, \tag{15}$$

where the numeric constant 3 in Eq. (15) is due to the 3 degrees of freedom of each atom. The projection operators for the translation and rotation of the cluster are defined accordingly and are, respectively, expressed as

$$P_j^T = \sum_{\alpha=T_x,T_y,T_z} P_j^\alpha \tag{16}$$

and

$$P_j^R = \sum_{\alpha=R_x,R_y,R_z} P_j^\alpha, \tag{17}$$

where (T_x,T_y,T_z) are the three translational INMs and (R_x,R_y,R_z) are either the three rotational INMs sorted out by method II or the purely rotational eigenvectors by method I. Additionally, one can calculate with P_j^α the jth atom contribution of the vibrational INM DOS which has $3n-6$ vibrational modes, viz.,

$$D_j(\omega) = \left\langle \frac{1}{3n-6} \sum_{\alpha=1}^{3n-6} P_j^\alpha \delta(\omega - \omega_\alpha) \right\rangle. \tag{18}$$

Obviously $D_j(\omega)$ is not normalized. With $D_j(\omega)$ so defined, the vibrational INM DOS of *all* atoms in the cluster, $D_{Vib}(\omega)$, satisfies another sum rule,

$$D_{Vib}(\omega) = \sum_{j=1}^{n} D_j(\omega). \tag{19}$$

Note that $D_j(\omega)$ includes also the real- and imaginary-frequency lobes. The integration of $D_j(\omega)$ over frequency yields, therefore,

$$I_j = \int D_j(\omega)d\omega = \int_0^\infty D_j^{(s)}(\omega)d\omega + \int_0^\infty D_j^{(u)}(\lambda)d\lambda = \frac{1}{3n-6}\left\langle \sum_{\alpha=1}^{3n-6} P_j^\alpha \right\rangle. \tag{20}$$

Since $D_j(\omega)$ is not normalized, I_j is not normalized. Thus, I_j is an ensemble average of all vibrational projection operators for the jth atom. Furthermore, due to the sum rule of P_j^α, I_j is governed moreover by the following equation:

$$I_j = \left\langle \frac{1}{3n-6} \sum_{\alpha=1}^{3n-6} P_j^\alpha \right\rangle = \frac{1}{3n-6}\left(3 - \left\langle P_j^T \right\rangle - \left\langle P_j^R \right\rangle\right), \tag{21}$$

which can easily be confirmed from Eqs. (15)–(17). We emphasize that I_j is a crucial quantity whose thermal variation sheds light on the melting behavior of a cluster that we will address below.

In the same vein, the individual atom $C^{(j)}(t)$ may be approximated as in Eq. (6) as

$$C^{(j)}(t) \approx \frac{1}{I_j}\int D_j(\omega)\cos(\omega t)d\omega = \frac{1}{I_j}\int_0^\infty D_j^{(s)}(\omega)\cos(\omega t)d\omega + \frac{1}{I_j}\int_0^\infty D_j^{(u)}(\lambda)\cosh(\lambda t)d\lambda. \tag{22}$$

In the stable-INM approximation, $C^{(j)}(t)$ is further reduced to

$$C_{\mathrm{INM,s}}^{(j)}(t) \approx \frac{1}{I_j^{(s)}}\int_0^\infty D_j^{(s)}(\omega)\cos(\omega t)d\omega, \tag{23}$$

where $I_j^{(s)} = \int_0^\infty D_j^{(s)}(\omega)d\omega$. After making the inverse cosine transform for Eq. (23), the jth atom power spectral density in the stable-INM approximation is given as $\Omega_{\mathrm{INM,s}}^{(j)}(\omega) \equiv \pi D_j^{(s)}(\omega)/I_j^{(s)}$ and it plays a similar role as that $\Omega^{(j)}(\omega)$ described above in Eq. (7). At low temperatures in the absence

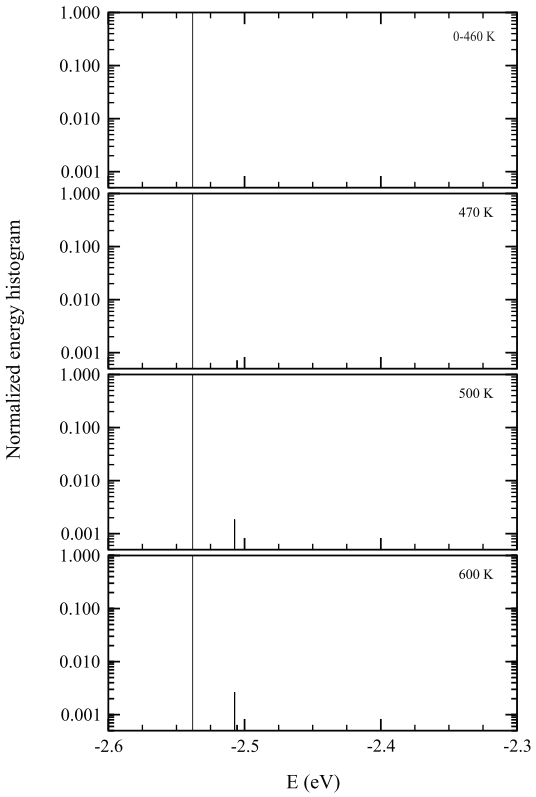

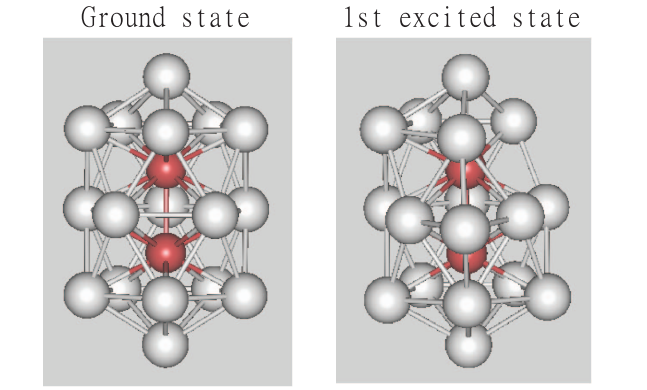

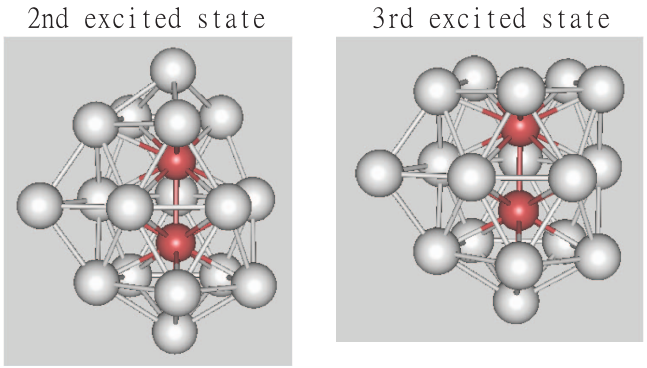

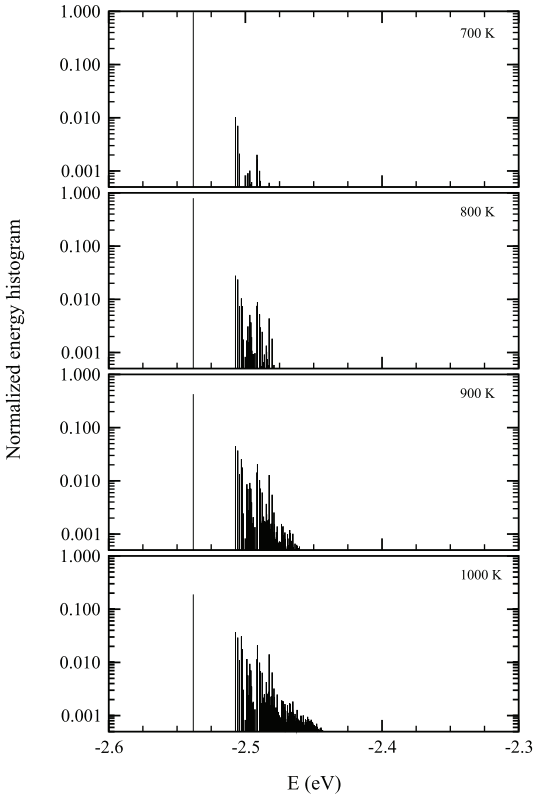

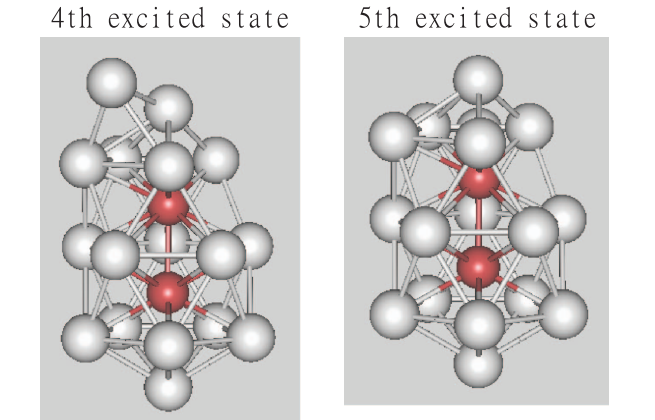

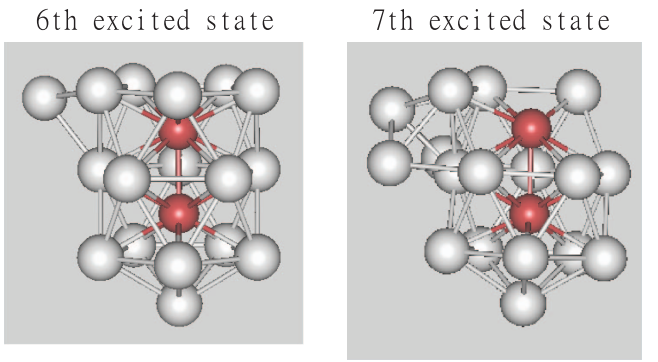

FIG. 1. Energy histograms and structures of the lowest, first, second, and higher minima for bimetallic cluster $Ag_{17}Cu_2$. Normalized energy histograms were constructed from isothermal Brownian-type MD simulations.

of imaginary-frequency INM, the two quantities $\Omega^{(j)}_{\mathrm{INM,s}}(\omega)$ and $\Omega^{(j)}(\omega)$ are expected to be equal.

The aforedescribed theory of INM is quite general and applicable to any cluster, pure or alloy, at any temperature. In Sec. III, we apply the INM analysis to the $Ag_{17}Cu_2$ cluster, which is thermally driven from low to high temperatures and shows how the predictions of the theory reveal the melting behavior.

III. RESULTS AND DISCUSSION

A. Structure and C_V for $Ag_{17}Cu_2$

We depict in Fig. 1 the normalized energy histogram and cluster geometries of $Ag_{17}Cu_2$. For $T < 460$ K, the BC is in its lowest energy state. The first lowest minimum appears at $T \approx 470$ K, and at this temperature, one of the Ag atoms in the (upper or lower) pentagonal ring moves to reside at a position near the middle pentagonal ring. This migrated Ag atom sits at a location above four Ag atoms which comprise one Ag atom from each of the upper and lower pentagonal rings and two from the middle pentagonal ring. Up to $T = 500$ K, only the lowest and first lowest minima are detected. The second lowest minimum emerges at $T = 600$ K after which we notice a rapid growth of higher lowest minima. Note in particular that the two Cu atoms, which are embedded inside the Ag atoms, continue to stay on interiorly up to the sixth lowest minimum.

In Fig. 2, we show the specific heat of $Ag_{17}Cu_2$ which is included for comparison of the C_V of $Ag_{12}Cu_1$. We read from this figure that the main maximum position of C_V, which we define to be the cluster's melting temperature, is located at $T_m \approx 890$ K. This melting temperature is lower than the C_V of 13-atom $Ag_{12}Cu_1$ ($T_m \approx 1000$ K). Thus we see that the double icosahedron $Ag_{17}Cu_2$, which has an elongated geometry and embeds two Cu atoms, is energetically less stable compared with $Ag_{12}Cu_1$.

B. VAF and power spectrum for $Ag_{17}Cu_2$

The temperature variations of the VAF and spectral density of $Ag_{17}Cu_2$ are displayed in Figs. 3(a)–3(c). Three features merit emphasis:

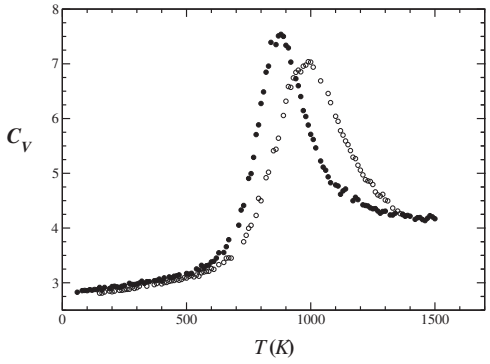

FIG. 2. Specific heat C_V of $Ag_{17}Cu_2$ (closed circle) and $Ag_{12}Cu_1$ (open circle) calculated using the isothermal Brownian-type MD simulation.

(a) Owing to the structural symmetry, the two Cu atoms $C^{(\mathrm{Cu})}(t)$ exhibit indistinguishable characteristics. They show robust oscillatory profiles at low T and these oscillatory behaviors gradually reduce in range as T increases up to $T \approx 500$ K. At $T > 500$ K, the oscillatory structures of $C^{(\mathrm{Cu})}(t)$ temper to a shorter time range. The $C^{(\mathrm{Ag})}(t)$ of surface atoms Ag, on the other hand, show strong solidlike oscillations for $T \lesssim 500$ K and above 500 K their $C^{(\mathrm{Ag})}(t)$ change to profiles characterized by single minima followed by damped decaying tails.

(b) The $\Omega^{(\mathrm{Cu})}(\omega)$ of Cu atoms have three conspicuous frequencies located at $\omega_L \approx 20$, $\omega_M \approx 40$, and $\omega_H \approx 45$ rad/ps. These frequency modes differ from the $\Omega^{(\mathrm{Ag})}(\omega)$ of surface atoms Ag whose frequencies spread over the range $5 \lesssim \omega \lesssim 25$ rad/ps centralizing around $\omega = 15$ rad/ps. It is interesting to note that the intensity of $\Omega^{(\mathrm{Cu})}(\omega)$ at $\omega = \omega_H$ of the Cu atom first increases at low temperatures (in the temperature range $T = 100 \rightarrow 200$ K), thereafter ($T > 200$ K) decreases and disappears identically at $800 < T \lesssim 900$ K. In marked contrast, the intensity of $\Omega^{(\mathrm{Cu})}(\omega)$ at $\omega = \omega_M$ shows no sign of diminishing even when $T > T_m \approx 890$ K. This unusual feature occurs also in $Ag_{12}Cu_1$ (see Figs. 4(a)–4(c)) and in our previous studies of 14-atom Ag-based BCs.[4]

(c) At $T > 600$ K all the $\Omega^{(\mathrm{Ag})}(\omega)$ of surface atoms Ag merge into a single frequency at $\omega^{(\mathrm{Ag})} \approx 15$ rad/ps. This $\omega^{(\mathrm{Ag})}$ is lower than the $\omega_L \approx 20$ rad /ps of the two Cu atoms. We note in particular a rise in $\Omega^{(\mathrm{Cu})}(\omega)$ and $\Omega^{(\mathrm{Ag})}(\omega)$ at $\omega \approx 0$, a scenario reminds us of the bulk liquidlike phase.

C. Instantaneous normal modes for $Ag_{17}Cu_2$

The Gupta potential used in the present work is a many-body empirical function. The derivation of the Hessian elements for $Ag_{17}Cu_2$, though straightforward, is rather cumbersome. The explicit expressions of essential equations are given in Appendix B. Our detailed INM analysis for $Ag_{17}Cu_2$ can be summarized as follows.

1. Temperature variation of the INM spectra

We begin by averaging over 10^6 configurations generated by the Brownian-type MD simulations with a time step of 10^{-15} s within a total interval of 10^{-8} s. At such a long time scale, the calculated $C(t)$ and all $C^{(i)}(t)$ even at $T = 100$ K have vanished already. Figure 5 depicts the normalized INM spectra of $Ag_{17}Cu_2$ with and without the rotational modes. In general, we find no noticeable difference at low T for the vibrational spectra obtained by the two methods described above to remove the rotational INMs. Slight difference is observed, however, at low frequencies at high T. Since the couplings between the rotational and vibrational degrees of freedom of the clusters which are thermally equilibrated with a heat bath substantially increase with temperature,[15] we consider mostly the vibrational INM obtained by method II in this paper, except for evaluations associated with the I_j values.

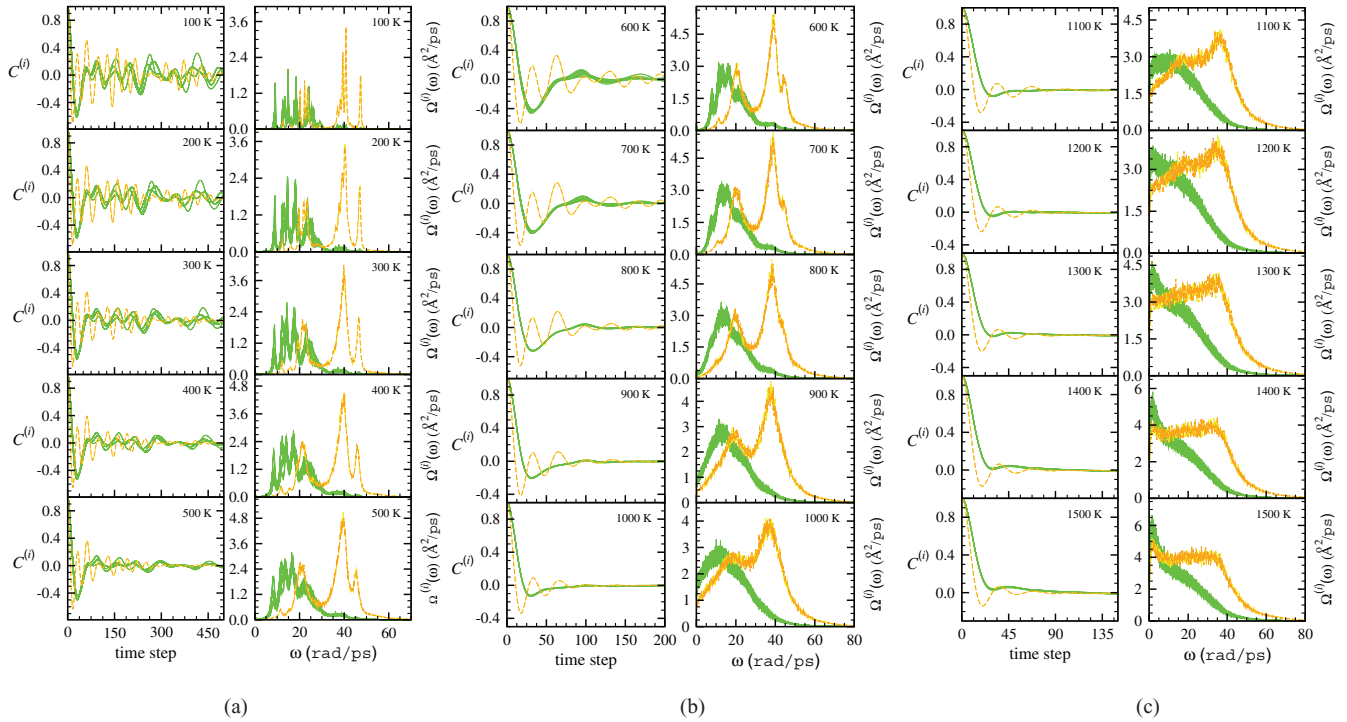

FIG. 3. (a) Temperature variation (100–500 K) of the velocity autocorrelation function (left column) vs. time step (in units of 5×10^{-15} s) and power spectrum (right column) vs. frequency ω (in units of rad/ps) for $Ag_{17}Cu_2$ obtained from the isothermal Brownian-type MD simulation. The curve is colored orange (dashed line) for center atom Cu, green (solid line) for the surface atoms Ag. (b) Same as 3(a) except for the temperature range (600–1000 K). (c) Same as 3(a) except for the temperature range (1100–1500 K).

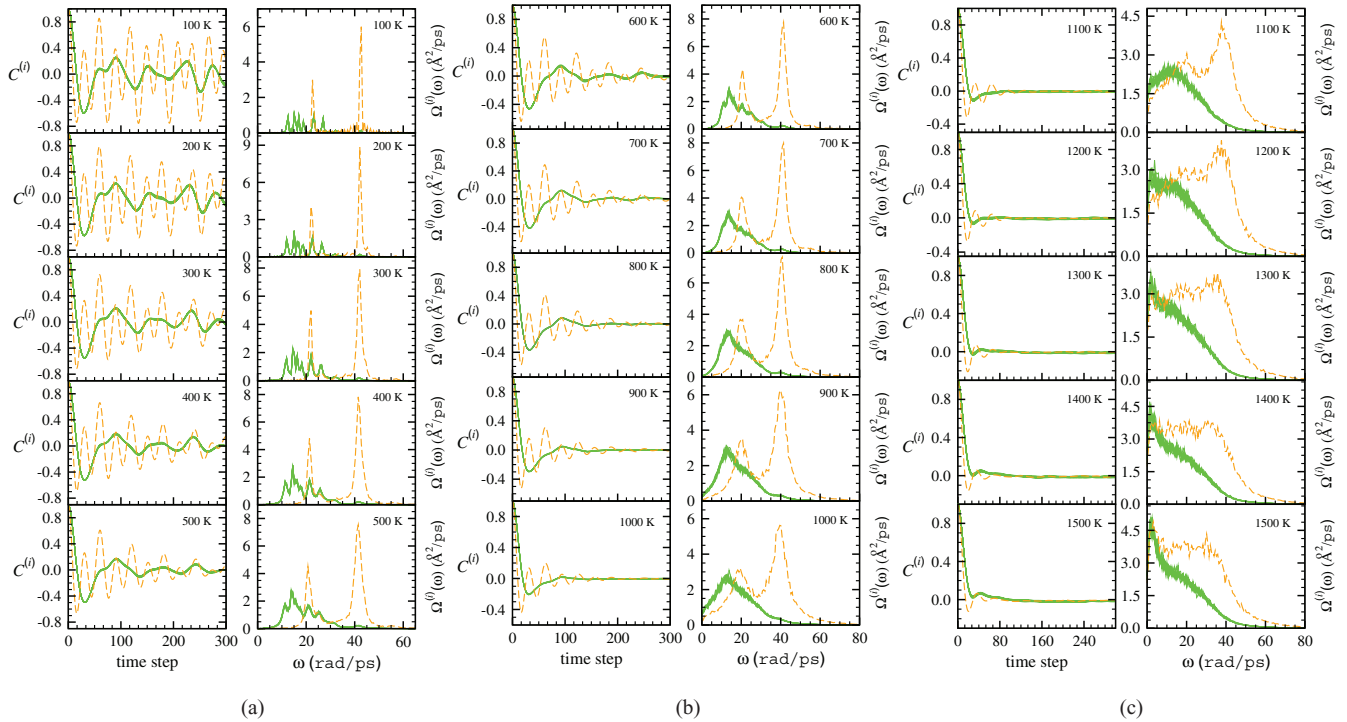

FIG. 4. (a) Temperature variation (100–500 K) of the velocity autocorrelation function (left column) vs. time step (in units of 5×10^{-15} s) and power spectrum (right column) vs. frequency ω (in units of rad/ps) for $Ag_{12}Cu_1$ obtained from the isothermal Brownian-type MD simulation. The curve is colored orange (dashed line) for center atom Cu, green (full line) for the surface atoms Ag. (b) Same as 4(a) except for the temperature range (600–1000 K). (c) Same as 4(a) except for the temperature range (1100–1500 K).

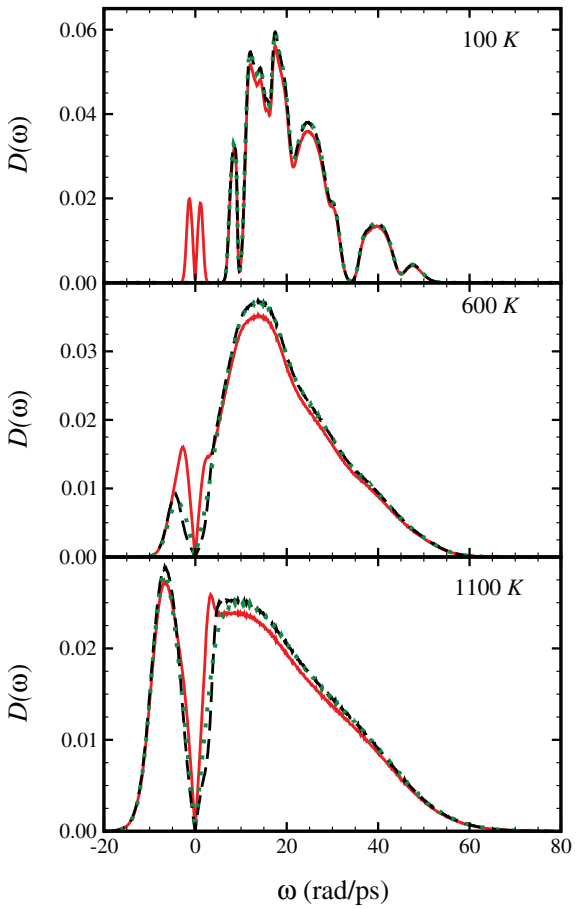

FIG. 5. Normalized INM spectra $D_{Vib}(\omega)$ of $Ag_{17}Cu_2$ at 100, 600, and 1100 K. The red-solid lines are the spectra showing the contributions of rotations and vibrations. The black-dashed and green-dotted lines are the spectra obtained by removing the rotational contribution following methods I and II, respectively.

At $T = 100$ K, the vibrational spectra show structural characteristics that all vibrational modes possess real frequencies, displaying indeed a solidlike picture. At this temperature, one would expect the configurations of the cluster to be around the lowest energy state of the potential energy landscape. As the temperature increases to 600 K, the INM spectra are generally smoothed out. Here we observe some vibrational modes with imaginary frequencies when the rotational modes are excluded. This result and the information from the energy histogram in Fig. 1 suggest a transition process in which the cluster at higher temperatures possesses enough kinetic energy to stray sufficiently far from the lowest energy state that enhances its chance to crossover the energy barriers to the first and higher lowest minima. As temperature is increased further to 1100 K, one noticeable feature is that the INM spectra display a large portion of imaginary-frequency vibrational INM and this structural trait is consistent with a liquidlike behavior, in which the cluster at sufficiently high temperatures would go around everywhere the potential energy landscape.

The temperature variations for the vibrational INM spectra of individual atoms are shown in Fig. 6. We note first of all that the spectra of the two Cu atoms are indiscernible on the scales used in Fig. 6 for all temperatures, with a general behavior which may be summarized as follows: At $T = 100$ K, we observe three main peaks located at $\omega \approx 23$, 40, and 48 rad/ps (cf. Sec. III B (b)) and a lower one at $\omega \approx 12$ rad/ps. The peaks at the highest and lowest frequencies are smeared out to become shoulders at $T = 200$ K and the latter completely disappear at $T = 300$ K. For the 17 Ag atoms, their spectra at $T = 100$ K spread mainly the frequency range from $\omega = 5$ to 35 rad/ps, with a separated minor structure appearing around 40 rad/ps, and they are in fact structurally discernible; these characteristic structures, however, get smudged as the temperature increases and gradually become blurred among atoms at much higher temperatures. One general feature that can be gleaned from Fig. 6 is that the imaginary-frequency INM DOS for both Cu and Ag atoms emerge at $T \approx 300$ K, become noticeable at $T \approx 600$ K for Cu atoms and 400 K for Ag atoms, and thereafter grow into a significant portion at much higher temperatures.

The comparison between $C^{(i)}(t)$ and its time Fourier-transformed, $\Omega^{(i)}(\omega)$, of individual atoms obtained by the INM theory and the simulation results are given in Figs. 7(a) and 7(b) for the Ag and Cu atoms, respectively. We have calculated $C^{(i)}(t)$ with the INM DOS using Eq. (22) and in the stable-INM approximation by Eq. (23). At $T = 100$ K, without any imaginary-frequency INM, the results of the INM theory and the stable-INM approximation are the same and the calculated $C^{(i)}(t)$ of both the Ag and Cu atoms are rather close to those obtained by simulations (see Figs. 7(a) and 7(b)). For the power spectra $\Omega^{(i)}(\omega)$, the locations of the peaks of the two kinds of atoms predicted by the INM theory generally coincide with those of the simulation results but they are much broader in width. At $T = 500$ K, because of the imaginary-frequency INMs, the $C^{(i)}(t)$ calculated by the INM theory deviates somewhat from the simulated results after 0.1 ps; the deviation is stronger for the Ag atom (Fig. 7(a)) than that for the Cu atom (Fig. 7(b)), due to more imaginary-frequency INM in the $D_j(\omega)$ of Ag atoms. At this temperature, the spike-like structures in the simulated $\Omega^{(i)}(\omega)$ are seen to be cut away in the INM theory. At $T = 900$ and 1500 K, the $C^{(i)}(t)$ calculated by the INM theory yields accurately the simulation results roughly within 80 fs, which is the same time scale for the cases of bulk liquids,[39,40] but diverges strongly in the long-time limit due to the imaginary-frequency INMs. It is worth mentioning that for the Ag-atom $C^{(i)}(t)$ at $T = 900$ K both the stable-INM approximation and the simulation result display an over-damped behavior over a long time scale. At the same temperature 900 K, the behavior of $C^{(i)}(t)$ obtained by simulations for the Cu atom is, however, under-damped in noticeable contrast to that in the stable-INM approximation showing too fast damping (see Fig. 7(b)).

2. Ground-state structure vibrational modes and classification of atoms

To understand the INM spectra of individual atoms in the cluster at $T = 100$ K, it is instructive to first examine the normal modes of the ground-state structure of $Ag_{17}Cu_2$ (see Fig. 1). The vibrational-mode DOS $D^{(G)}_{Vib}(\omega)$ of the ground-state structure that excludes the translational and

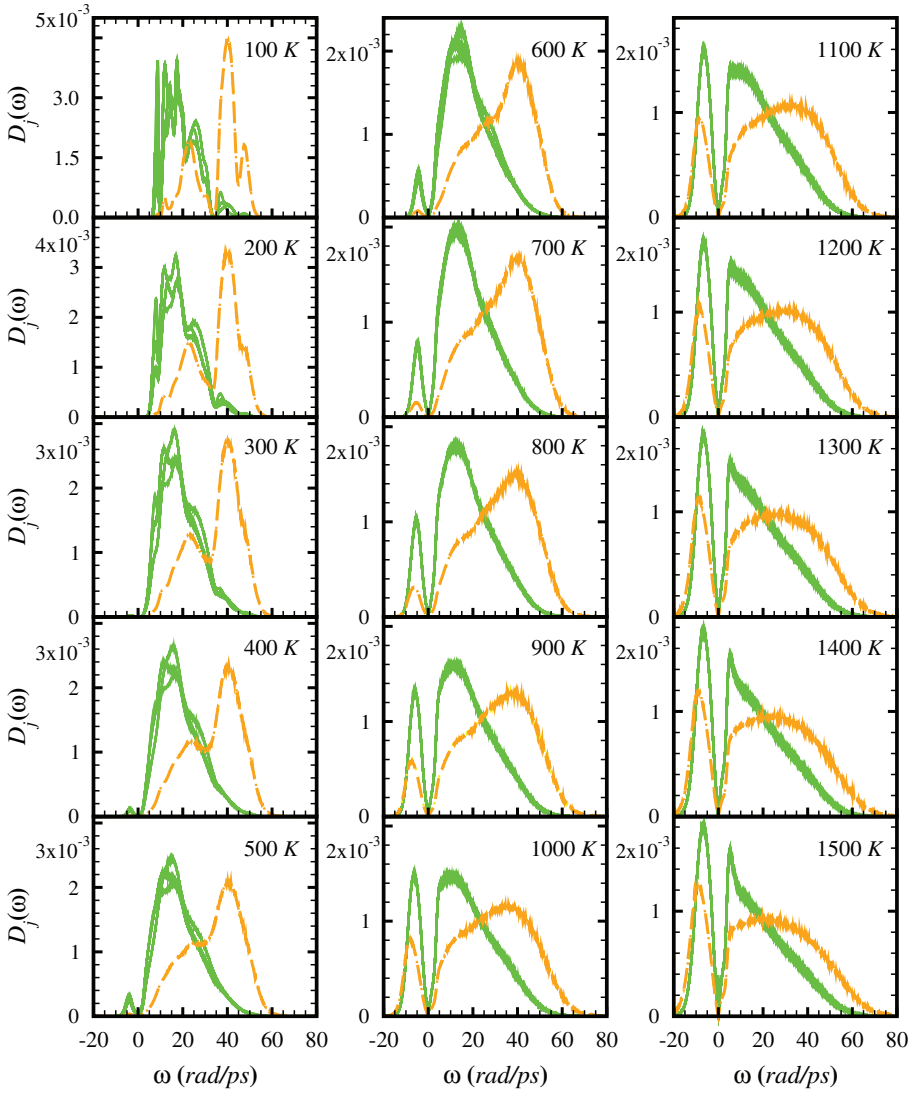

FIG. 6. Temperature variation of the vibrational INM spectra $D_j(\omega)$ of atoms from 100 to 1500 K. The spectra are obtained by the method II described in the text. The dashed lines (orange) are for Cu atoms and the full lines (green) are for Ag atoms.

rotational modes reads

$$D_{Vib}^{(G)}(\omega) = \sum_{\beta=1}^{3n-6} \delta_{\omega,\omega_\beta},$$

where ω_β is the βth vibrational-mode frequency pertaining to the ground-state configuration and the symbol $\delta_{\omega,\omega_\beta}$ is the Kronecker delta. As shown in Fig. 8(a), the vibrational-mode DOS uncovers the degeneracy of each vibrational frequency. Consider the ground-state structure of $Ag_{17}Cu_2$ shown in Fig. 1. The cluster has the D_{5h} symmetry[41] with the principal axis that goes along the two centrally located Cu atoms, i.e., C_5 symmetry, a reflection symmetry about the plane containing the middle pentagonal ring, i.e., σ_h symmetry and another reflection symmetry about the plane containing the principal axis and any one of the Ag atoms residing at the middle pentagonal ring, i.e., σ_v symmetry. Due to the D_{5h} point group, the vibrational frequencies are either non-degenerate or doubly degenerate.

The normal-mode eigenvectors of $Ag_{17}Cu_2$ in its ground-state structure can similarly be used to define the projection operator of atom j,

$$P_j^{\beta,(G)} = \left|\vec{e}_j^{\beta,(G)}\right|^2,$$

where $\vec{e}_j^{\beta,(G)}$ is the three-dimensional jth atom projection vector in the βth vibrational mode. The same definition applies to the translational and rotational projection operators, which are denoted as $P_j^{T,(G)}$ and $P_j^{R,(G)}$, respectively. Furthermore these projection operators can be employed to calculate the jth atom vibrational DOS in the ground-state configuration and we have (cf. Eq. (18))

$$D_j^{(G)}(\omega) = \frac{1}{3n-6} \sum_{\beta=1}^{3n-6} P_j^{\beta,(G)} \delta_{\omega,\omega_\beta}.$$

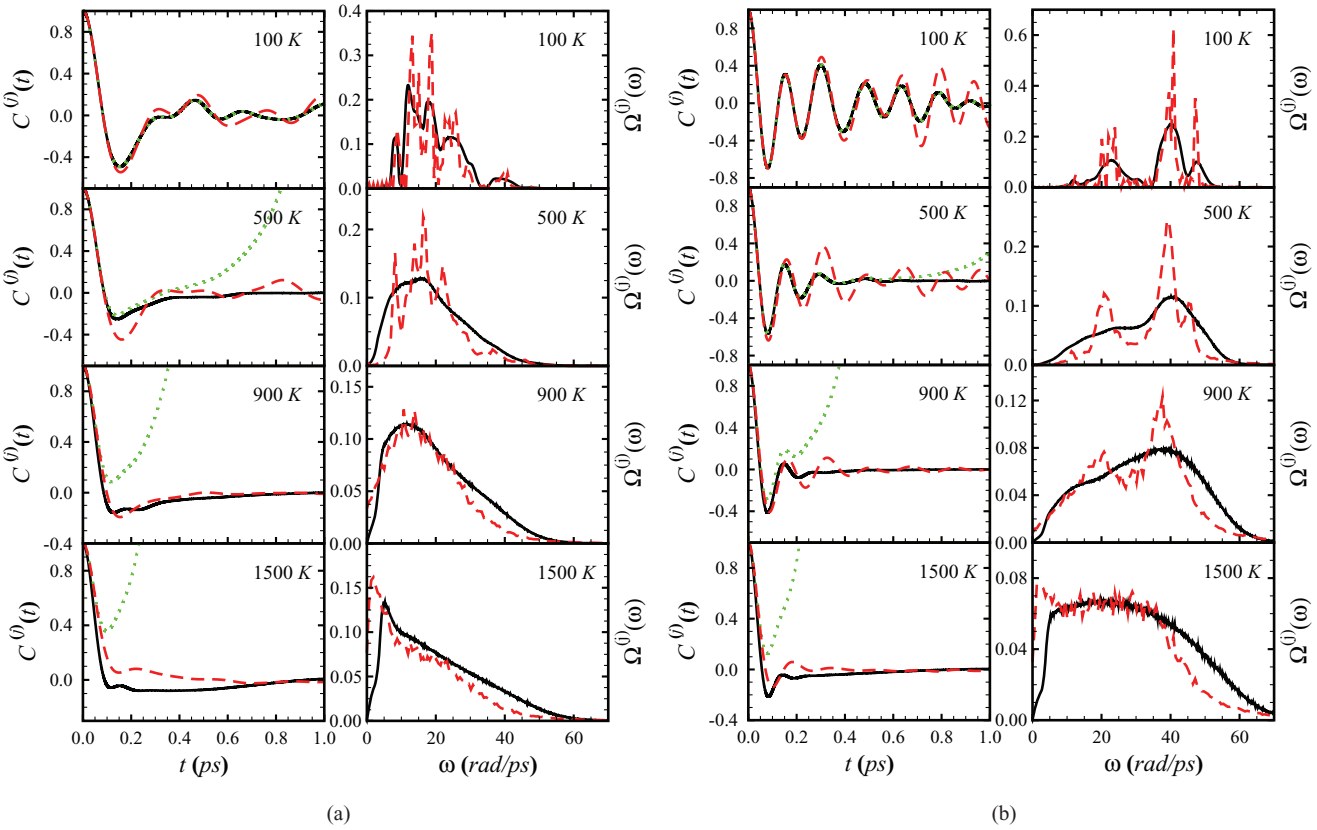

FIG. 7. (a). VAF $C^{(j)}(t)$ and power spectrum $\Omega^{(i)}(\omega)$ of an Ag atom at 100, 500, 900, and 1500 K. The Ag atom is one in the subset $Ag^{(10)}$ [see Fig. 8(b)]. For $C^{(j)}(t)$ and $\Omega^{(i)}(\omega)$, the full lines are the results calculated in the stable-INM approximation and the dashed lines are the results from MD simulations (Fig. 3(a)). The dotted lines in $C^{(j)}(t)$ are results calculated with both real- and imaginary-frequency INMs. All vibrational INM spectra used in the calculations are obtained by method II. (b). Same as 7(a) except for a Cu atom in the $Cu^{(2)}$ subset (see Fig. 8(b)).

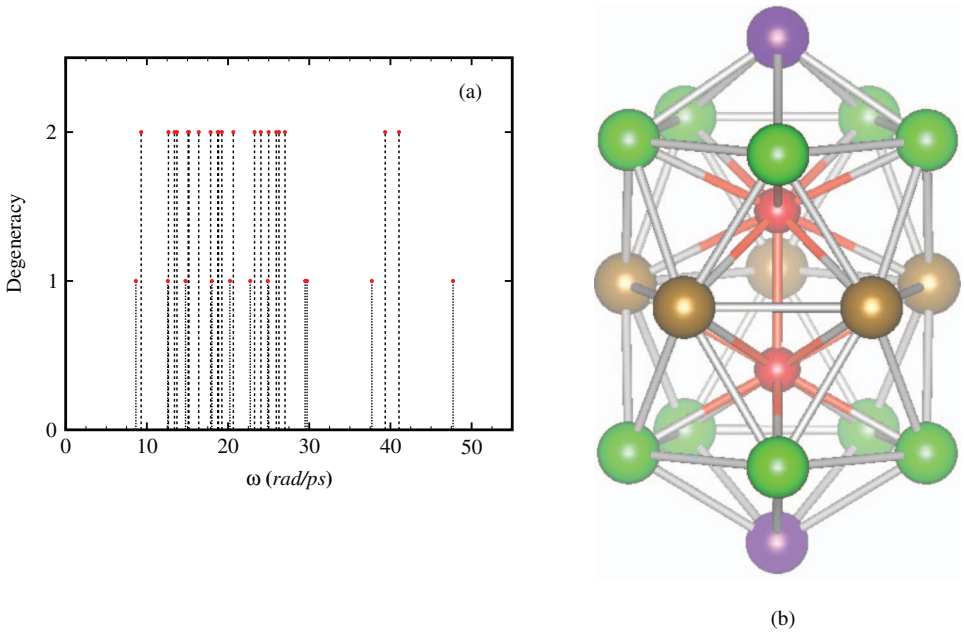

FIG. 8. (a) The vibrational instantaneous normal mode frequencies and (b) the four subsets of atoms of the $Ag_{17}Cu_2$ cluster in its ground-state structure. The four subsets of atoms are: $Cu^{(2)}$, two Cu atoms (red); $Ag^{(2)}$, top and bottom Ag atoms (violet); $Ag^{(5)}$, five Ag atoms occupying the middle pentagonal ring (brown); $Ag^{(10)}$, ten Ag atoms sitting in the upper and lower pentagonal rings (green).

The integration of $D_j^{(G)}(\omega)$ over all frequencies leads accordingly to

$$I_j^{(G)} = \int D_j^{(G)}(\omega)d\omega = \frac{1}{3n-6}\sum_{\beta=1}^{3n-6} P_j^{\beta,(G)},$$

which can easily be shown to satisfy

$$I_j^{(G)} = \frac{3-\left(P_j^{T,(G)}+P_j^{R,(G)}\right)}{3n-6}.$$

To make further progress, we delve into the symmetry operations of the ground-state structure, which, as pointed out above, assume D_{5h} point group. In this lowest energy geometry, the transformation matrices for the atom positions are reducible into four diagonal blocks, with each block corresponding to a subset of atoms. The 19 atoms of the cluster are thus classified into four subsets. Figure 8(b) shows these subsets consisting of the two centrally located Cu atoms, top and bottom Ag atoms, five Ag atoms occupying the middle pentagonal ring, and ten Ag atoms sitting in the upper and lower pentagonal rings which we denote hereafter as $Cu^{(2)}$, $Ag^{(2)}$, $Ag^{(5)}$, and $Ag^{(10)}$, respectively. In this classification, the atoms in a subset possess the same symmetry and their $D_j^{(G)}(\omega)$ is thus the same.

In the same manner, the atoms in the $Ag_{17}Cu_2$ cluster at finite temperatures can be classified into four subsets according to the following procedure: A chosen number of atoms at a finite temperature can be obtained from those at the lowest energy state by tracing the atom labels in the simulation at a temperature that is raised gradually from zero. After this simulation process of temperature raising, we identify the atoms by their original subsets at zero temperature. At low temperatures, one can sensibly recognize the four subsets of atoms by the structures of the cluster, since the relative positions of atoms are roughly the same as those at zero temperature. Thus, the classification of atoms into the four subsets generally reflects the structures of the cluster at low temperatures. This is not so at high temperatures where the cluster is more appropriately realized by the liquidlike picture with its atoms of the same mass becoming completely random so that the subsets of atoms of $Ag^{(2)}$, $Ag^{(5)}$, and $Ag^{(10)}$ lose the identities they had at zero temperature. As a result, atoms at high temperatures are only distinguishable by their masses.

Owing to the same response of atoms in a subset, we make an average of $D_j(\omega)$ for atoms in the same subset, i.e.,

$$D_X(\omega) = \frac{1}{n_X}\sum_{j=1}^{n_X} D_j(\omega),$$

with the subscript $X = Cu^{(2)}$, $Ag^{(2)}$, $Ag^{(5)}$, and $Ag^{(10)}$ and j runs for the total number of n_X atoms in subset X. The $D_X(\omega)$ is, therefore, considered as the averaged contribution of one atom in subset X to all vibrational INM with frequency ω.

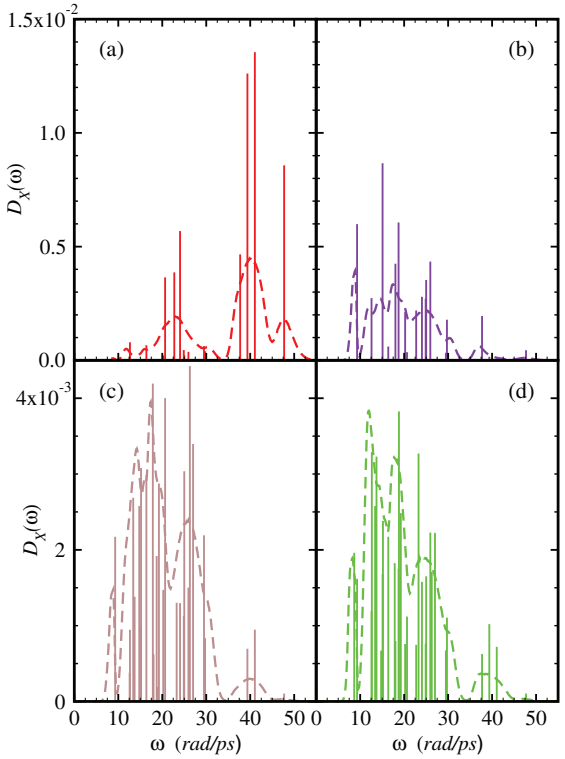

FIG. 9. Vibrational DOS $D_X(\omega)$ of subsets X, with (a) $X = Cu^{(2)}$, (b) $X = Ag^{(2)}$, (c) $X = Ag^{(5)}$, and (d) $X = Ag^{(10)}$. The delta lines and dashed curves refer to the $Ag_{17}Cu_2$ cluster in the ground-state configuration and at $T = 100$ K, respectively.

3. INM spectra of a subset of atoms and temperature variations of I_j

We present in Fig. 9 the $T = 100$ K instantaneous normal mode $D_X(\omega)$ for the four subsets of atoms of the $Ag_{17}Cu_2$ cluster and in the same figure for the INM $D_X^{(G)}(\omega)$ at the ground-state structure. It can be seen that $D_X^{(G)}(\omega)$ is a bundle of delta functions. Considering $D_X^{(G)}(\omega)$ in Fig. 9(a), its vibrational modes above $\omega = 37$ rad/ps are dominated by Cu atoms whose four $D_X^{(G)}(\omega)$ have the highest values. This is in contrast to the modes shown in Ag atoms (Figs. 9(b)–9(d)) with $\omega < 30$ rad/ps whose $D_X^{(G)}(\omega)$ are dominant. A comparison between $D_X(\omega)$ and $D_X^{(G)}(\omega)$ of each subset of atoms indicates a general feature of the temperature effects for transposing the vibrational spectrum from delta functions into a continuous function. Indeed, due to the thermal effects, the vibrational frequency gap at $T = 100$ K between $\omega = 30$ and 37 rad/ps in $D_X^{(G)}(\omega)$ is gradually filled up in the $D_X(\omega)$, but there is an exception at $\omega = 35$ rad/ps where all the $D_X(\omega)$ are identically zero.

We are now in a position to study the temperature variations of I_j for the four subsets of atoms. In the upper part of Fig. 10, the I_j, which is calculated with the vibrational INM that follows method II, is plotted at a temperature increment of 10 K from $T = 10$ to 1500 K and, at each T, we average over 10^6 configurations. The I_j values of the $Cu^{(2)}$ subset of atoms are almost constant at low temperatures and, around 500 K, start to decrease gradually with increasing temperature. This declining behavior of the I_j of $Cu^{(2)}$ is well separated from

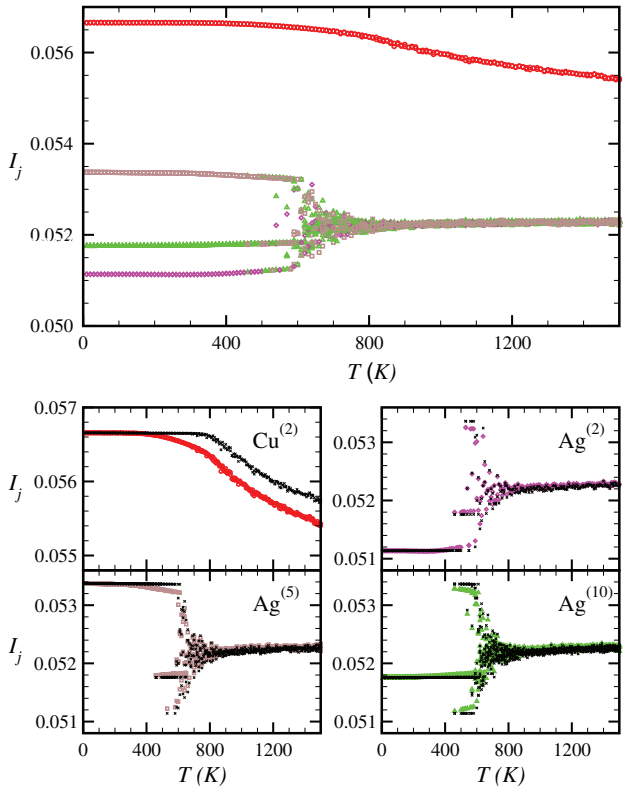

FIG. 10. Temperature variations of I_j for the atoms in the four subsets: $Cu^{(2)}$ (red circles), $Ag^{(2)}$ (magenta diamonds), $Ag^{(5)}$ (brown squares), and $Ag^{(10)}$ (green triangles) (see Fig. 8(b)). The I_j values in the upper panel are obtained from the vibrational INM by method II. In the lower four panels, each figure compares the I_j of a subset of atoms with its vibrational INM obtained by method I (black crosses) and that by method II (same symbols as in the upper panel).

those other three subsets of Ag atoms for the range of temperature considered here due to the difference in masses of Ag and Cu atoms. In the lower part of Fig. 10, we compare the I_j of each subset of atoms calculated with the vibrational INM applying either method I or method II. It is evident that the calculated results by the two methods for the three subsets of Ag atoms are rather similar. On the other hand, we find that both I_j of $Cu^{(2)}$ subset of atoms obtained by the two methods exhibit similar temperature behavior and coincide at low temperatures but are well separated at high temperatures, with the temperature change for the I_j value by method I starting to decrease around 800 K.

It is interesting to see in the upper part of Fig. 10 that the I_j of the three subsets of Ag atoms split into three tracks below 450 K and, as $T \rightarrow 0K$, the I_j values of the three subsets of atoms converge to the values of $I_j^{(G)}$ defined above. From $T = 450$ to 600 K, the three tracks of the subsets of Ag atoms are still visibly separated. These well-resolved tracks are, however, somewhat defiled by exchanges between two tracks which correspond physically to site permutations between Ag atoms (for examples, $Ag^{(2)} \leftrightarrow Ag^{(10)}$ and $Ag^{(5)} \leftrightarrow Ag^{(10)}$). Between $T = 600$ and 900 K, the I_j of the three subsets of Ag atoms start to mix interchangeably and the tracks are no longer discernible. The I_j gradually lose the identities of the original subsets of atoms with increasing temperature. After $T = 900$ K, the I_j of all Ag atoms merge into one so that the cluster is distinguished by two I_j corresponding to a thorough mixing of the two Cu atoms and among the Ag atoms.

We delve further into the dynamics of Ag atoms by the I_j temperature variation of each subset of Ag atoms illustrated in the lower part of Fig. 10. Below $T = 450$ K, the structures of the three subsets of Ag atoms mimic that of the ground-state structure implying that these atoms possibly vibrate with small amplitudes about their solidlike equilibrium positions. From $T = 450$ to 600 K, the thermal variation of the I_j of each subset of Ag atoms indicates that the Ag atoms are undergoing sites exchange between subsets of atoms whose structures remain dynamically similar to those of the ground state configuration. In this temperature segment, it is also possible that the three subsets of atoms of Ag atoms are displaced in their sites and driven to the first and the second lowest minima by thermal activations over the barriers in the potential energy landscape; the probabilities of these thermal crossovers are indicated by the energy histograms in Fig. 1. At much higher temperatures falling between $T = 600$ and 900 K, the probability to surmount energy barriers into even higher energy states increases and such large probabilities indicate that the cluster at this point will stray far from the lowest energy structure. Correspondingly, within this temperature range, the C_V shown in Fig. 2 increases dramatically and reaches a maximum at $T = 900$ K. Above $T = 900$ K, there is only a small probability of finding the cluster in the ground state; the solidlike structure could have "melted," with the Ag atoms completely indistinguishable under an ensemble average, and as a result the C_V undergoes a sharp drop with the temperature increasing further.

In physics, the melting phenomena are commonly described by some appropriately chosen order parameters. In bulk systems, the first-order melting transition is characterized by a discontinuous jump in the order parameter, which can be C_V at the melting temperature, whereas in finite-sized systems such as clusters the same kind of transition is featured by a continuous change of C_V with temperature and it embodies the coexistence of the solidlike and liquidlike isomers.[25,28,42,43] Several other order parameters have been reported also and applied to understand the solidlike to liquidlike transition in clusters. On the issue of coexisting solidlike-liquidlike isomers, the microcanonical ensemble simulations[20,21,23,44] have associated the bimodality in the probability distribution of the short-time averaged temperature as *prima facie* evidence. These simulation studies have aroused subsequent interest in finding the solidlike and liquidlike states separated by a barrier in the Landau free energy, and the potential energy then serves as the order parameter of the free energy.[45] Parallel to appealing to the energy order parameters, the geometric order parameters that base upon the short-time average are used as well for addressing the transition between two stable isomers and their coexistence,[46] and also the bond-orientational order parameters for investigating the structural variation along pathways in configuration space.[47,48] We should perhaps mention more over the continual use of the root-mean-square bond length fluctuation constant δ as a Lindemann-like order parameter in more recent computer simulations.[29,31,49] Despite the

drastic change of this order parameter with temperature indicating some kind of structural or phase transformation in bulk systems, the information of the transition deduced from δ for clusters is, however, not always consistent[30,49] with that inferred from C_V thus lending less credence to choosing δ as an order parameter to study phase transition.

Within the context of the INM analysis developed above, we propose a new order parameter $\tau(T)$ to describe the melting transition of clusters. Toward this goal, we refer to Eq. (21) and write the variance of I_j for the 17 Ag atoms at each T as

$$\sigma_I^2(T) = \left[\frac{1}{n_{Ag}} \sum_{j=1}^{n_{Ag}} I_j^2 - \left(\frac{1}{n_{Ag}} \sum_{j=1}^{n_{Ag}} I_j \right)^2 \right],$$

where $n_{Ag} = 17$. The order parameter $\tau(T)$ is defined as the standard deviation $\sigma_I(T)$ normalized at $T = 0$. In other words,

$$\tau(T) = \frac{\sigma_I(T)}{\sigma_I(0)}.$$

The calculated $\tau(T)$ is shown in Fig. 11. With the I_j values obtained by method II, $\tau(T)$ is almost one below $T = 300$ K signaling that the ground-state structure is well preserved. From $T = 300$ to 600 K, $\tau(T)$ declines from 1 to 0.85 which again indicates that the ground-state structure is generally maintained. The $\tau(T)$ starts to drop sharply at $T \approx 600$ K and approaches asymptotically to a small value at a temperature close to $T_m \approx 890$ K. This sharply decaying range of $\tau(T)$ marks a melting shake-up of the ground-state structure. The $\tau(T)$ stays constant at temperatures $T > T_m$ and is non-zero due to the finite size of the cluster. Physically, it describes the atomic distributions that, under ensemble averages, exhibit no further distinction among the Ag atoms at much higher (than T_m) temperatures. Thus, the phenomenon of cluster melting described by $\tau(T)$ is consistent with the thermal behavior of C_V shown in Fig. 2. Except for the constant one extending up to ~600 K, the temperature variation of $\tau(T)$ calculated from the I_j values following either method I or method II is quite similar. This result indicates that the decline of $\tau(T)$ from $T = 300$ to 600 K by method II is related to the rotation-vibration coupling in the $Ag_{17}Cu_2$ cluster via the Gupta potential.

In recapitulation, we remark that the INM averages in $\tau(T)$ are carried out for the configurations that evolve along the long-time cluster trajectories, and that the underlying statistical average for the order parameter is based upon the canonical ensemble at each temperature. Though under different statistical averages, the indication of $\tau(T)$ for the transition of cluster melting are complementary to those obtained by another INM analysis under the short-time average in the microcanonical ensemble.[44]

IV. CONCLUSIONS

We performed the isothermal Brownian-type molecular dynamics to calculate the velocity autocorrelation function, and its time Fourier-transformed power spectral density. These quantities were analyzed and the dynamical behavior of individual atoms as a function of temperature, the power spectral density, in particular, was examined. We found that the highest frequency mode $\Omega^{(Cu)}(\omega_H)$ of the Cu atom, which is located at $\omega_H \approx 45$ rad/ps, disappears identically at a temperature within $800 < T \lesssim 900$ K. This temperature was used to infer the melting temperature of the $Ag_{17}Cu_2$ cluster, which we define at $T_m \approx 890$ K corresponding to the main peak position of C_V. The dynamical properties of $Ag_{17}Cu_2$ were further diagnosed using the INM analysis. In addition to the vibrational mode DOS agreeing favorably with the simulation results, we observe that the frequency integrated value I_j which is an ensemble average of all vibrational projection operators for the jth atom in the cluster changes with temperature in a characteristic manner that sheds considerable light on the melting behavior. A detailed examination of the I_j of Ag atoms leads furthermore to a new order parameter $\tau(T)$. The INM analysis shows that $\tau(T)$ contains cluster dynamic information and also predicts the T_m of $Ag_{17}Cu_2$ reasonably close to that inferred from C_V. In view of this finding, the $\tau(T)$ derived in this work is a promising order parameter for understanding the cluster thermal property as well. Further exploration of the order parameter $\tau(T)$ is, therefore, worthwhile.

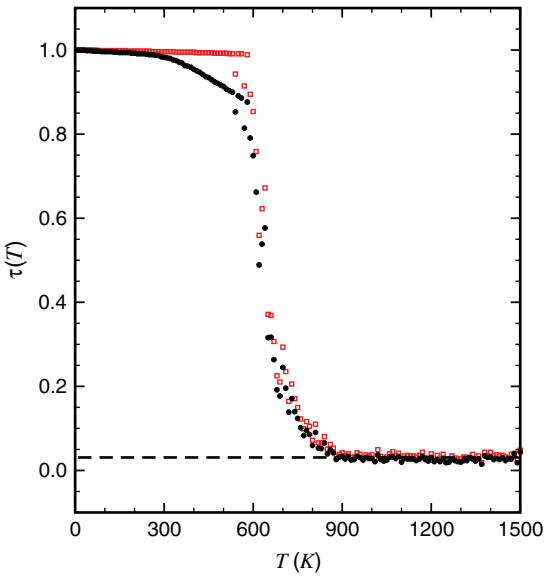

FIG. 11. Order parameter $\tau(T)$ *vs* temperature T (K) calculated with the I_j values of Ag atoms (shown in Fig. 10) obtained by method I (open squares) or method II (filled circles). The dashed line is the asymptotic high-T value of $\tau(T)$.

ACKNOWLEDGMENTS

This work is supported by the National Science Council, Taiwan (NSC 99-2112-M-008-001 (SKL) and NSC 99-2112-M-009-003-MY2 (TMW)). We are grateful to the National Center for high-performance computing for computer time and facilities.

APPENDIX A: PURELY ROTATIONAL NORMALIZED EIGENVECTORS

To calculate the purely rotational eigenvectors, we consider first a cluster assuming configuration $\boldsymbol{R}$, which may be

generated by a simulation in the laboratory frame. Then, the position coordinates of n atoms, which define the configuration $\boldsymbol{R}$, are first transformed into the body frame of the cluster. In this frame, the origin is at the center-of-mass and its coordinate axes coincide with the principal axes of the cluster. Next, for given atomic Cartesian coordinates r'_{jx}, r'_{jy}, and r'_{jz}, $(j = 1, \ldots, n)$ in the body frame, the three purely rotational normalized eigenvectors of configuration $\boldsymbol{R}$ are straightforwardly computed as

$$\vec{e}_j^{R'_x} = \sqrt{\frac{m_j}{I_x}} \begin{pmatrix} 0 \\ -r'_{jz} \\ r'_{jy} \end{pmatrix}, \quad \vec{e}_j^{R'_y} = \sqrt{\frac{m_j}{I_y}} \begin{pmatrix} r'_{jz} \\ 0 \\ -r'_{jx} \end{pmatrix},$$

$$\vec{e}_j^{R'_z} = \sqrt{\frac{m_j}{I_z}} \begin{pmatrix} -r'_{jy} \\ r'_{jx} \\ 0 \end{pmatrix},$$

where

$$I_\mu = \sum_{j=1}^{n} m_j \left(r'^2_{j\nu} + r'^2_{j\eta}\right)$$

are the moments of inertia that are defined with respect to the three principal axes. The subscripts $\mu \neq \nu \neq \eta$ are, as usual, assumed cyclic in x, y, and z.

APPENDIX B: HESSIAN MATRIX ELEMENTS OF THE GUPTA POTENTIAL

For simplicity, we rewrite the many-body empirical Gupta potential[32] in the form,

$$E_n(\boldsymbol{R}) = \sum_{i=1}^{n} \sum_{j=1(j\neq i)}^{n} u_{ij}(r_{ij}) - \sum_{i=1}^{n} U_i^{1/2}, \tag{B1}$$

where

$$u_{ij}(r) = A_{ij} \exp\left[-p_{ij}\left(\frac{r}{r_{ij}^{(0)}} - 1\right)\right] \tag{B2}$$

and

$$U_i = \sum_{j=1(j\neq i)}^{n} \phi_{ij}(r_{ij}) \tag{B3}$$

in which

$$\phi_{ij}(r) = \xi_{ij}^2 \exp\left[-2q_{ij}\left(\frac{r}{r_{ij}^{(0)}} - 1\right)\right]. \tag{B4}$$

The first and second terms of $E_n(\boldsymbol{R})$ describe pairwise and many-body interactions, respectively. The Hessian matrix elements $K_{j\mu,k\nu}(\boldsymbol{R})$ of the Gupta potential can be calculated by Eq. (8). For the pairwise interactions, they have been given previously,[8,13] but for the many-body interactions the derivation of the Hessian matrix elements is, however, complicated. Here, we give only the explicit expressions, which are

$$K_{j\mu,k\nu}(\boldsymbol{R}) = \begin{cases} \dfrac{-1}{\sqrt{m_j m_k}} W_{j\mu,k\nu}(\boldsymbol{R}), & j \neq k, \\ \dfrac{1}{m_j} \displaystyle\sum_{l=1(l\neq j)}^{n} W_{j\mu,l\nu}(\boldsymbol{R}), & j = k, \end{cases} \tag{B5}$$

where

$$W_{j\mu,k\nu}(\boldsymbol{R}) = 2(\overleftrightarrow{T}_{jk}(\vec{r}_{jk}))_{\mu\nu} - \frac{1}{2}\left(U_j^{-1/2} + U_k^{-1/2}\right)(\overleftrightarrow{S}_{jk}(\vec{r}_{jk}))_{\mu\nu} - \sum_{\substack{p=1 \\ (p\neq j, p\neq k)}}^{n} G_{jkp}(\overleftrightarrow{R}_{jkp})_{\mu\nu} + \sum_{p=1(p\neq k)}^{n} G_{jpk}(\overleftrightarrow{R}_{jpk})_{\mu\nu} + \sum_{p=1(p\neq j)}^{n} G_{pkj}(\overleftrightarrow{R}_{pkj})_{\mu\nu}. \tag{B6}$$

The first and second terms in $W_{j\mu,k\nu}(\boldsymbol{R})$ involve two particles and the last three terms involve three particles. For the two-body terms in $W_{j\mu,k\nu}(\boldsymbol{R})$, $(\overleftrightarrow{T}_{jk}(\vec{r}_{jk}))_{\mu\nu}$, and $(\overleftrightarrow{S}_{jk}(\vec{r}_{jk}))_{\mu\nu}$ are the elements of 3×3 tensors which can be calculated readily as

$$\overleftrightarrow{T}_{jk}(\vec{r}) = \frac{u'_{jk}(r)}{r} \overleftrightarrow{I}_3 + \left(u''_{jk}(r) - \frac{u'_{jk}(r)}{r}\right) \hat{r}\hat{r}, \tag{B7}$$

$$\vec{S}_{jk}(\vec{r}) = \frac{\phi'_{jk}(r)}{r} \overleftrightarrow{I}_3 + \left(\phi''_{jk}(r) - \frac{\phi'_{jk}(r)}{r}\right) \hat{r}\hat{r}, \tag{B8}$$

where $\hat{r} = \vec{r}/|\vec{r}|$ and $\hat{r}\hat{r}$ is a 3×3 tensor and the prime and double-prime on $u_{jk}(r)$ and $\phi_{jk}(r)$ mean the first and second r derivatives, respectively. Also, $\overleftrightarrow{I}_3$ is a 3×3 unit tensor. In contrast, for the three-body terms in $W_{j\mu,k\nu}(\boldsymbol{R})$, j and k denote the root particles and p $(\neq j, k)$ is a field particle, which is one to be summed. The quantity $(\overleftrightarrow{R}_{jkp})_{\mu\nu}$ is an element of the 3×3 tensor $\overleftrightarrow{R}_{jkp} \equiv \hat{r}_{jp}\hat{r}_{kp}$ whose transpose, $\overleftrightarrow{R}_{jkp}{}^{\dagger}$, satisfies $\overleftrightarrow{R}_{jkp}{}^{\dagger} = \overleftrightarrow{R}_{kjp}$. Finally the quantity G_{jkp} is a three-body scalar function, which is related to $\phi_{jk}(r)$ as

$$G_{jkp} \equiv G_{jkp}(r_{jp}, r_{kp}) = \frac{U_p^{-3/2}}{4} \phi'_{jp}(r_{jp}) \phi'_{kp}(r_{kp}). \tag{B9}$$

Obviously, we have $G_{jkp} = G_{kjp}$. We shall apply Eq. (B5) to determine the INM.

[1] P. J. Hsu and S. K. Lai, J. Chem. Phys. **124**, 044711 (2006).
[2] G. Rossi, A. Rapallo, C. Mottet, A. Fortunelli, F. Baletto, and R. Ferrando, Phys. Rev. Lett. **93**, 105503 (2004).
[3] A. Rapallo, G. Rossi, R. Ferrando, A. Fortunelli, B. C. Curley, L. D. Lloyd, G. M. Tarbuck, and R. L. Johnston, J. Chem. Phys. **122**, 194308 (2005).
[4] T.-W. Yen, P. J. Hsu, and S. K. Lai, e-J. Surf. Sci. Nanotechnol. **7**, 149 (2009).
[5] R. M. Stratt, Acc. Chem. Res. **28**, 201 (1995).
[6] T. Keyes, J. Phys. Chem. A **101**, 2921 (1997).
[7] B. Madan, T. Keyes, and G. Seeley, J. Chem. Phys. **92**, 7565 (1990).
[8] T. M. Wu and R. F. Loring, J. Chem. Phys. **97**, 8568 (1992); Y. Wan and R. M. Stratt, J. Chem. Phys. **100**, 5123 (1994).
[9] S. D. Bembenek and B. B. Laird, Phys. Rev. Lett. **74**, 936 (1995); J. Chem. Phys. **104**, 5199 (1996).
[10] R. Schulz, M. Krishnan, I. Daidone, and J. C. Smith, Biophys. J. **96**, 476 (2009); C. Peng, L. Zhang, and T. Head-Gordon, Biophys. J. **98**, 2356 (2010).
[11] D. J. Wales, *Energy Landscapes, With Applications to Clusters, Biomolecules and Glasses* (Cambridge University Press, Cambridge, England, 2003).
[12] D. J. Wales and T. V. Bogdan, J. Phys. Chem. B **110**, 20765 (2006).
[13] J. E. Adams and R. M. Stratt, J. Chem. Phys. **93**, 1332 (1990).
[14] J. E. Adams and R. M. Stratt, J. Chem. Phys. **93**, 1358 (1990).
[15] J. E. Adams and R. M. Stratt, J. Chem. Phys. **93**, 1632 (1990).
[16] F. H. Stillinger and T. A. Weber, Science **225**, 983 (1984).

[17]F. H. Stillinger and T. A. Weber, Phys. Rev. A **25**, 978 (1982); Phys. Rev. A **28**, 2408 (1983).
[18]G. Natanson, F. Amar, and R. S. Berry, J. Chem. Phys. **78**, 399 (1983); R. S. Berry, J. Jellinek, and G. Natanson, Phys. Rev. A **30**, 919 (1984).
[19]F. G. Amar and R. S. Berry, J. Chem. Phys. **85**, 5943 (1986).
[20]J. Jellinek, T. L. Beck, and R. S. Berry, J. Chem. Phys. **84**, 2783 (1986).
[21]T. L. Beck, J. Jellinek, and R. S. Berry, J. Chem. Phys. **87**, 545 (1987).
[22]H. L. Davis, J. Jellinek, and R. S. Berry, J. Chem. Phys. **86**, 6456 (1987).
[23]T. L. Beck and R. S. Berry, J. Chem. Phys. **88**, 3910 (1988).
[24]T. L. Beck, D. M. Leitner, and R. S. Berry, J. Chem. Phys. **89**, 1681 (1988).
[25]R. S. Berry and D. J. Wales, Phys. Rev. Lett. **63**, 1156 (1989).
[26]D. J. Wales and R. S. Berry, J. Chem. Phys. **92**, 4473 (1990).
[27]D. J. Wales and R. S. Berry, J. Chem. Phys. **92**, 4283 (1990).
[28]D. J. Wales and R. S. Berry, Phys. Rev. Lett. **73**, 2785 (1994).
[29]S. K. Lai, W. D. Lin, K. L. Wu, W. H. Li, and K. C. Lee, J. Chem. Phys. **121**, 1487 (2004).
[30]T.-W. Yen, S. K. Lai, N. Jakse, and J. L. Bretonnet, Phys. Rev. B **75**, 165420 (2007).
[31]P. J. Hsu, J. S. Luo, S. K. Lai, J. F. Wax, and J. L. Bretonnet, J. Chem. Phys. **129**, 194302 (2008).
[32]R. P. Gupta, Phys. Rev. B **23**, 6265 (1981).
[33]C. Mottet, G. Treglia, and B. Legrand, Phys. Rev. B **46**, 16018 (1992).
[34]D. A. McQuarrie, *Statistical Mechanics* (Harper & Row, New York, 1976).
[35]R. E. Larsen, G. Goodyear, and R. M. Stratt, J. Chem. Phys. **104**, 2987 (1996).
[36]M. Page and J. W. Mclver, J. Chem. Phys. **88**, 922 (1988).
[37]T. M. Wu and R. F. Loring, J. Chem. Phys. **99**, 8936 (1993).
[38]M. Buchner, B. M. Ladanyi, and R. M. Stratt, J. Chem. Phys. **97**, 8522 (1992).
[39]T. M. Wu and S. F. Tsay, J. Chem. Phys. **105**, 9281 (1996).
[40]T. M. Wu, S. L. Chang, S. F. Tsay, and K. H. Tsai, J. Non-Cryst. Solids **352**, 4615 (2006).
[41]R. L. Carter, *Molecular Symmetry and Group Theory* (Wiley, New York, 1998).
[42]D. J. Wales and J. P. K. Doye, J. Chem. Phys. **103**, 3061 (1995).
[43]M. Schmidt, R. Kusche, W. Kronmüller, B. von Issendorff, and H. Haberland, Phys. Rev. Lett. **79**, 99 (1997); M. Schmidt, R. Kusche, B. V. Issendorff, and H. Haberland, Nature (London) **393**, 238 (1998); H. Schmidt and H. Haberland, C. R. Phys **3**, 327 (2002).
[44]D. J. Wales, J. Chem. Soc. Faraday Trans. **87**, 2399 (1991).
[45]R. M. Lynden-Bell and D. J. Wales, J. Chem. Phys. **101**, 1460 (1994).
[46]J. P. K. Doye and D. J. Wales, J. Chem. Phys. **102**, 9673 (1995).
[47]D. J. Wales, J. Chem. Phys. **101**, 3750 (1994).
[48]F. Calvo, Phys. Rev. E **82**, 046703 (2010).
[49]F. Calvo and F. Spiegelmann, J. Chem. Phys. **112**, 2888 (2000).